# **Ligand Engineering for Precise Control of Strongly-Confined CsPbI<sub>3</sub> Nanoplatelet Superlattices for Efficient Light-Emitting Diodes**

Jongbeom Kim<sup>1,†</sup>, Woo Hyeon Jeong<sup>2,3,†</sup>, Junzhi Ye<sup>3\*</sup>, Allison Nicole Arber<sup>4</sup>, Vikram<sup>4</sup>, Donghan Kim<sup>1</sup>, Yi-Teng Huang<sup>3,5</sup>, Yixin Wang<sup>3</sup>, Dongeun Kim<sup>1</sup>, Dongryeol Lee<sup>1</sup>, Chia-Yu Chang<sup>3</sup>, Xinyu Shen<sup>6</sup>, Sung Yong Bae<sup>3</sup>, Ashish Gaurav<sup>3</sup>, Akshay Rao<sup>7</sup>, Henry J. Snaith<sup>6</sup>, M. Saiful Islam<sup>4\*</sup>, Bo Ram Lee<sup>2\*</sup>, Myoung Hoon Song<sup>1\*</sup> Robert L. Z. Hoye<sup>3\*</sup>

<sup>&</sup>lt;sup>1</sup>Department of Materials Science and Engineering, Ulsan National Institute of Science and Technology (UNIST), Ulsan, 44919 Republic of Korea

<sup>&</sup>lt;sup>2</sup>School of Advanced Materials Science and Engineering, Sungkyunkwan University, Suwon, 16419, Republic of Korea

<sup>&</sup>lt;sup>3</sup>Inorganic Chemistry Laboratory, University of Oxford, Oxford, OX1 3QR, United Kingdom

<sup>&</sup>lt;sup>4</sup>Department of Materials, University of Oxford, Oxford, OX1 3PH, United Kingdom

<sup>&</sup>lt;sup>5</sup>Graduate Institute of Photonics and Optoelectronics and Department of Electrical Engineering, National Taiwan University, Taipei 10617, Taiwan

<sup>&</sup>lt;sup>6</sup>Clarendon Laboratory, Department of Physics, University of Oxford, Oxford, OX1 3PU United Kingdom

<sup>&</sup>lt;sup>7</sup>Cavendish Laboratory, University of Cambridge, Cambridge CB3 0US, United Kingdom

<sup>&</sup>lt;sup>†</sup>These authors contributed equally.

<sup>\*</sup>Correspondence: junzhi.ye@chem.ox.ac.uk (J.Y.), saiful.islam@materials.ox.ac.uk (M.S.I.), brlee@skku.edu (B.R.L.), mhsong@unist.ac.kr (M.H.S.), robert.hoye@chem.ox.ac.uk (R.L.Z.H.)

# **ABSTRACT**

Strongly-confined perovskite nanoplatelets (PeNPLs) offer promising opportunities for photonics and optoelectronics due to their narrowband emission, control over the transition dipole moment, and potential for polarized light emission. However, achieving uniform PeNPLs and effective surface passivation major challenges, especially for red-emitting iodide-based compounds. Here, we address these challenges with an ancillary ligand engineering strategy. Combining experimental and ab-initio modelling techniques, we demonstrate that ligands possessing an optimal backbone with strong surface binding and Pb-coordination not only passivate defects, but also improve thickness uniformity. The PeNPLs self-assemble into superlattices a single emission peak, indicative of uniform monolayer formation and orientation-dependent optical properties. Uniform-monolayer PeNPLs obtained with benzylphosphonic acid (BPAc) self-assemble into well-ordered superlattices with orientationdependent optical properties. Face-down PeNPL thin films fabricated with solvent engineering exhibit Lambertian-like emission suitable for light-emitting devices, while edge-up oriented films exhibit linearly polarized emission. When integrated into light-emitting diodes, our PeNPL devices achieve a external quantum efficiency of 13.1%, the highest reported for strongly-confined PeNPL-based devices. Taken together, these results establish ancillary ligand-induced synthesis of uniform-monolayer PeNPLs as a decisive route to robust orientation control, positioning it as the central principle for advancing next-generation photonic and display technologies.

**Keywords:** perovskite nanoplatelets, linearly polarized light emission, superlattice, nanocrystal growth control, light-emitting diode

# **MAIN**

Colloidal semiconducting nanocrystals (NCs) offer advantages for optics and photonics, as well as for fundamental investigations of light-matter properties<sup>1, 2, 3</sup>. To fully realize these benefits, it is critical to achieve highly monodisperse NCs, which requires precise control over nucleation and growth via well-regulated reaction conditions<sup>4, 5, 6, 7, 8</sup>. Among these materials, lead halide perovskite nanocrystals (PNCs), with the general formula APbX<sub>3</sub> (A = formamidinium, methylammonium, Cs; X = Cl, Br, I), have emerged as one of the most promising, due to their narrow full-width at half-maximum (FWHM), defect tolerance, and the ability to achieve high luminescence quantum yields with cost-effective solution processing methods<sup>9, 10, 11, 12</sup>. In particular, two-dimensional perovskite nanoplatelets (PeNPLs), which can be classified by the number of monolayers (MLs) of lead-halide octahedra, exhibit a tunable emission wavelength due to quantum and dielectric confinement effects<sup>13, 14</sup>. Furthermore, their anisotropy in their confinement leads to exciton fine structure splitting, which can enable linearly polarized light emission<sup>15, 16, 17</sup>.

Despite these exciting properties, PeNPLs face significant challenges in their realization of efficient and stable LEDs. Their inherently fast reaction kinetics, stemming from their ionic nature and low formation energy, makes it difficult to achieve uniform nanoplatelet thicknesses<sup>18, 19, 20</sup>. This results in a distribution of emission wavelengths that compromise optical properties, such as colour saturation and degree of linear polarization<sup>21, 22</sup>. Such limitations represent a fundamental bottleneck for the entire class of NPLs, since achieving colloidal uniformity and structural stability is essential for realizing their fully exploit their optoelectronic potential<sup>27</sup>.

For the synthesis and dispersion of PeNPLs, long chain organic ligands such as oleate (OA<sup>-</sup>) and oleylammonium (OAm<sup>+</sup>) are commonly used<sup>28, 29, 30</sup>. While these native ligands play a crucial role in PeNPL synthesis, their weak surface binding affinity leads to dynamic ligand desorption, resulting in poor colloidal stability and surface defect formation, including halide vacancies and uncoordinated Pb ions<sup>31, 32, 33</sup>. These defects can lead to aggregation between PeNPLs or decomposition, ultimately deteriorating the structural integrity of uniform-ML PeNPLs. This instability is further exacerbated during thin film formation, as ligand desorption accelerates, diminishing both the stability and optical properties of PeNPLs<sup>34, 35</sup>. Moreover, these insulating ligands severely hinder charge-carrier transport and injection, making them unsuitable for high-performance LED applications<sup>33, 36</sup>. Therefore, for the rational design of red-emitting iodide-based PeNPLs in high-performance optoelectronic devices, it is essential to develop monodisperse uniform-ML PeNPLs while implementing advanced passivation strategies to overcome the limitations posed by native ligands. To address these limitations, it is crucial to develop strategies that not only enable the synthesis of monodisperse PeNPLs with uniform-ML thickness but also enhance surface passivation by employing ligands tailored for both colloidal monodispersity and device integration.

To overcome these challenges, we introduce an ancillary ligand-induced synthesis approach for CsPbI<sub>3</sub> PeNPLs to precisely control the nucleation and growth of CsPbI<sub>3</sub> PeNPLs. This involves introducing addition Lewis base ligands to bind to the perovskite surface in addition to the oleate and oleylammonium baseline ligands. The critical determinants of the ancillary ligand are the backbone structure and Pb-coordination strength with the halide perovskite surface. Combining density functional theory (DFT) with nuclear magnetic resonance measurements, the optimal backbone structure and strong coordination between ancillary ligand and Pb precursors effectively modulates crystal growth kinetics, enabling the formation of uniform 3ML-thick PeNPLs while simultaneously passivating surface defects. Importantly, although only a small fraction of OA/OAm ligands are replaced by the ancillary benzylphosphonic acid (BPAc), this modest incorporation produces significant improvements in both crystal growth regulation and defect passivation, underscoring its decisive impact without requiring full surface substitution. The resulting BPAc-incorporated CsPbI<sub>3</sub> PeNPLs (BPAc-PeNPLs) exhibits high ML purity, self-assemble into well-ordered superlattices, and demonstrate significantly enhanced optical properties, including higher photoluminescence quantum yield and extended carrier lifetimes. In addition, BPAc-PeNPLs maintain homogeneous and single emission after film formation owing to their well-passivated surfaces, as confirmed by transient absorption spectroscopy and confocal PL microscopy. Furthermore, the controlled orientation of BPAc-PeNPLs in the thin-film state enables versatile applications depending on their alignment. Edge-up oriented PeNPL thin films exhibit superior linear polarization properties due to uniform dipole alignment, with the degree of polarization increasing from 3.6% in pristine-PeNPLs thin films to 11.8% in BPAc-PeNPL thin films. Conversely, face-down oriented PeNPLs enhance outcoupling in the normal direction in LEDs, leading to high external quantum efficiency (EQE) reaching 13.1%. This is significantly higher than that of the pristine-PeNPL device (2.4%), representing the highest reported value for strongly-confined colloidal PeNPLbased LEDs. Taken together, our results establish ancillary ligand-induced synthesis of uniform-ML PeNPLs as the decisive route to robust orientation control, defining orientation engineering as the key principle for advancing strongly confined PeNPLs toward next-generation photonic and display technologies.

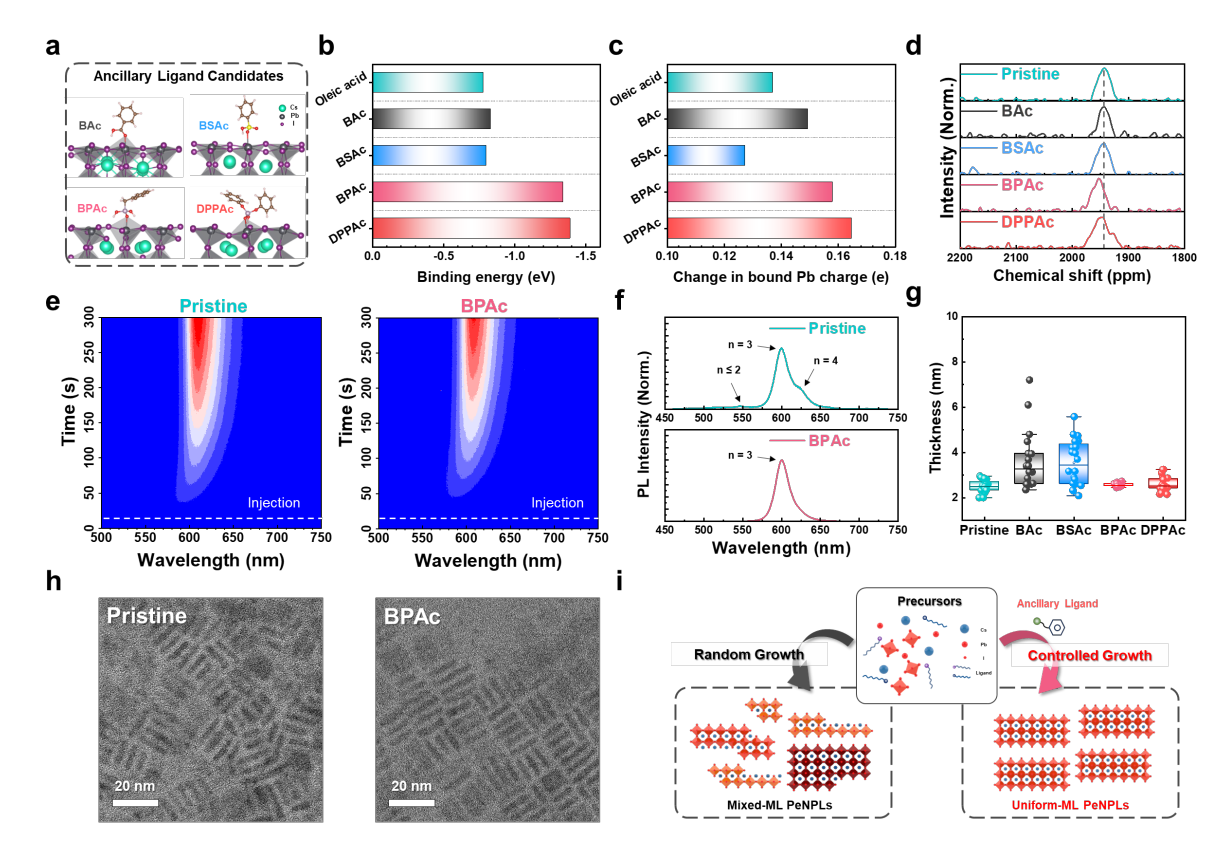


Fig. 1 | Controlled synthesis of well-ordered uniform-monolayer CsPbI<sub>3</sub> PeNPLs with ancillary ligands

a Candidate ligands for ancillary ligand-induced synthesis bound to the perovskite surface. **b** Calculated binding energy of ligands on the perovskite surface. **c** Calculated charge on the surface Pb atom bound to the ligand molecule referenced to the charge of an unbound surface Pb atom. These charges increase upon binding which correlates to the deshielding of Pb observed by nuclear magnetic resonance (NMR). **d** Solution state <sup>207</sup>Pb NMR spectra of PbI<sub>2</sub> precursor solutions without and with ancillary ligands. **e** *Insitu* photoluminescence spectra recorded during synthesis under ambient air conditions, excited with a 405 nm CW laser (37.3 mW cm<sup>-2</sup>). **f** Photoluminescence spectra of pristine-PeNPL and BPAc-PeNPL colloidal solutions. **g** Thickness distribution histogram of each PeNPLs determined from TEM measurements from Fig. 1h and Supplementary Fig. 6. **h** High-resolution transmission electron microscopy (TEM) images of edge-up oriented pristine-PeNPLs and BPAc-PeNPLs. These nanoplatelets were dispersed in a hexane solvent and drop-cast onto a Cu TEM grid. **i** Schematic illustration of conventional synthesis and ancillary ligand-induced synthesis for PeNPLs.

# **RESULTS**

# Atomistic insights into ligand-Pb binding and controlled growth of uniform PeNPLs

We hypothesized that the growth of PeNPLs proceeds via a precursor (monomer)-ML conversion

pathway, wherein the introduction of strongly coordinating agents with the precursor can retard the conversion of precursors to PeNPLs, thus enabling regulation of crystallization and control over the final thickness of the PeNPLs. Especially Pb precursor is the main component to consider for regulating ML which is defined by the number of  $PbX_6$  (X = halide) octahedra<sup>37</sup>. In addition, the backbone of the ligands can influence the growth kinetics via steric hindrance<sup>38</sup>. Guided by this hypothesis, we investigated a range of ligands including benzoic acid (BAc), benzene sulfonic acid (BSAc), benzyl phosphonic acid (BPAc) which have functional groups to coordinate with  $Pb^{2+}$  and diphenyl phosphate (DPPAc) which have different backbone structure to investigate critical factors for controlled growth. The ancillary ligand candidates are illustrated in **Fig. 1a**.

Understanding the interactions between Pb precursors and coordinating ligands at the atomic scale is critical for elucidating how crystallization can be regulated. Prior to experimental investigation, density functional theory (DFT) calculations were performed to provide atomistic insights into the crystallization pathway and to clarify the role of specific ligands (Computational details in Methods). The surface-ligand calculations show that DPPAc and BPAc have the highest binding energies ( Fig. 1b) on the perovskite surface. The strength of binding can be related to the degree of PbI<sub>6</sub> octahedral distortion simulated at the surface as well as the bond length between the surface and the ligand molecules. DPPAc and BPAc are found to induce the highest degree of structural dist ortion, and both have the shortest Pb-O bond length of 2.46 Å compared to 2.63 Å for oleic aci d, the weakest-bound ligand. Bader charge analysis shows that electrons are transferred from the perovskite surface to the ligand molecule. The degree of charge transfer correlates with the strength of the binding interaction, with the largest charge transfer found for BPAc and DPPAc (Fig. 1c). These results indicate that BPAc and DPPAc, relatively, have stronger binding with surface Pb and thus greater potential to regulate crystal growth. To further characterize the ligand-precursor interactions underlying this growth modulation, we performed solution state 207Pb nuclear magnetic resonance (NMR) spectroscopy of the PbI<sub>2</sub> precursor solutions with and without an ancillary ligand. The <sup>207</sup>Pb NMR chemical shift is highly sensitive to the coordination environment of Pb<sup>2+</sup> ions<sup>39</sup>. As shown in Fig. 1d, the BPAc and DPPAc containing precursors exhibit a clear chemical shift from 1943.4 ppm (pristine) to 1953.2 ppm and 1949.7 ppm, indicating strong coordination of BPAc and DPPAc to Pb<sup>2+</sup> in line with the binding energy calculations. This shift supports the hypothesis that BPAc and DPPAc which have P=O functional group binds tightly to surface Pb<sup>2+</sup>, thereby reducing the availability of free Pb precursors during nucleation and growth. Overall, the ab-initio simulations and NMR measurements reveal new atomic-scale structural and mechanistic insights, which help to select the most effective ancillary ligand. Such ligand-metal interactions effectively moderate the supersaturation level, slowing down the overall reaction kinetics and promoting the formation of monodisperse, well-ordered PeNPLs.

Based on such the atomic-scale insights, we synthesized colloidal CsPbI<sub>3</sub> PeNPLs using the LARP method (detailed in **Methods**). Five types of samples were prepared for comparison: pristine-PeNPLs synthesized without ancillary ligand (pristine-PeNPLs) and ancillary ligand (BAc, BSAc, BPAc and DPPAc) incorporated PeNPLs (BAc-PeNPLs, BSAc-PeNPLs, BPAc-PeNPLs and DPPAc-PeNPLs). To elucidate the mechanism by which ancillary ligands regulate PeNPL growth, we conducted in-situ photoluminescence (PL) measurements during synthesis. A 405 nm continuous-wave (CW) laser was used as an excitation source, and the PL spectra were recorded at XX s time intervals. As shown in Fig. 1e and Supplementary Fig. 1-2, pristine-PeNPLs exhibited a rapid onset of PL signal followed by a gradual redshift in emission wavelength, indicating the formation of mixed ML populations through uncontrolled nucleation and growth. By comparison, BA- and BSAc-PeNPLs developed PL emission faster, reaching saturation within 250 s before declining, indicating that BSAc failed to retard crystal growth and instead destabilized the reaction dynamics. In contrast, BPAc- and DPPAc-PeNPLs displayed a delayed PL onset and a slower spectral shift, suggesting suppressed nucleation and more regulated crystal growth dynamics. This trend is quantified in Supplementary Fig. 3, which plots the evolution of the PL peak wavelength as a function of reaction time. Pristine-, BA- and BSA-PeNPLs showed a fast redshift from ~580 to 609 nm, while BPAc- and DPPAc-PeNPLs gradually evolved from 570 to 608 nm, indicating more controlled lateral and vertical growth. Additionally, the PL intensity profiles during the early reaction stages (Supplementary Fig. 4) reveal that BPAc- and DPPAc-PeNPLs exhibit a slower intensity rise compared to other samples. These observations suggest that BPAc and DPPAc ancillary ligand slow down both the nucleation rate and the subsequent crystal growth kinetics. Fig. 1f and Supplementary Fig. 5 shows the ultraviolet-visible absorption and PL spectra of the resulting PeNPL dispersions. Given that the out-of-plane dimensions of the PeNPLs are smaller than the Bohr diameter of CsPbI<sub>3</sub> (~12 nm<sup>40</sup>), the optical properties of these nanocrystals are strongly influenced by quantum confinement effects. The absorption spectra of all PeNPL samples exhibit a pronounced excitonic peak, directly confirming strong quantum confinement. Furthermore, pristine-PeNPLs exhibit multiple PL peaks centered at 550, 600, and 627 nm, corresponding to nanoplatelets with n = 2, 3, and 4 MLs in thickness (n is the number of monolayer)<sup>13</sup>, respectively. These multiple emission peaks indicate poor thickness uniformity, which is a known challenge in PeNPL systems, given that these PeNPLs are achieved under kinetically controlled growth conditions, rather than thermodynamic growth conditions. Along the multiple emission peaks, even the PL peak centered at 680 nm, corresponding to nanoplatelets with  $n \ge 5$  MLs has appeared in BAc-, BSAc- and DPPAc-PeNPLs. In contrast, BPAc-PeNPLs exhibit a single, sharp emission peak at 600 nm (FWHM ~ 21 nm), consistent with the formation of uniform 3ML-thick nanoplatelets. The absorption spectra further corroborate this observation, with the absence of higher or lower energy transitions confirming the suppression of undesired thickness variants. To further validate the morphological and structural

uniformity, high-resolution transmission electron microscopy (HR-TEM) was performed on edge-up oriented PeNPLs (**Fig. 1g-h** and **Supplementary Fig. 6**) and face-down oriented PeNPLs (**Supplementary Figs. 7-8**). Each PeNPL samples exhibited rectangular shapes with lateral sizes around 17 nm. However, BPAc-PeNPLs demonstrated significantly improved uniformity. Detailed HR-TEM analysis revealed thicknesses of  $2.50 \pm 0.29$  nm for pristine-PeNPLs,  $3.63 \pm 0.12$  nm for BAc-PeNPLs,  $3.54 \pm 0.98$  nm for BSAc-PeNPLs,  $2.57 \pm 0.06$  nm for BPAc-PeNPLs, and  $2.64 \pm 0.39$  nm for DPPAc-PeNPLs.

The significantly narrower thickness distribution in BPAc-PeNPLs directly reflects enhanced monodispersity, consistent with the optical results. Overall experimental results indicate that BPAc successfully regulates the growth of PeNPLs and results in uniform PeNPLs. However, this is consistent with our expectations that both DPPAc and BPAc containing P=O groups have high potential to regulate the growth of PeNPLs at the atomic-scale insight. To understand the discrepancy between these two ligands, we conducted <sup>1</sup>H NMR to characterize the surface chemistry of BPAc- and DPPAc-PeNPLs (Supplementary Fig. 9). Ferrocene (0.5 mg/mL) was introduced into each PeNPLs solution in DMSOd<sub>6</sub> as an internal reference for quantitative analysis. In the NMR spectra, the resonance at 4.17 ppm is assigned to ferrocene, the signal at 5.33 ppm corresponds to the vinylic protons (-HC=CH-) of the native ligands<sup>41, 42</sup>. Quantitative integration of these peaks relative to ferrocene shows that DPPAc-PeNPLs have significantly decreased amounts of native ligands than pristine- and BPAc-PeNPLs. This tendency originated from the backbone of DPPAc. The bulky backbone hinders the attachment of native ligand on perovskite surface at the stage of growth and washing, finally leading to colloidal instability, following diminishing formation of uniform thickness PeNPLs while dispersion. Overall results in Figure 1 underscore two notable conclusions. First, the incorporation of functional groups such as P=O, which exhibit strong binding to Pb, is crucial for regulating crystal growth and thereby enabling the synthesis of uniform-ML PeNPLs. Second, even when crystal growth is effectively controlled, the steric bulk of ancillary ligands can modulate the surface chemistry and, in turn, alter the ML of the resulting PeNPLs.

Based on the understanding of the nucleation and growth kinetics of ancillary ligand incorporation, to investigate the impact of BPAc ligand on optical properties of PeNPLs, we performed photoluminescence quantum yield (PLQY) and time-resolved photoluminescence (TRPL) measurements for both pristine-PeNPLs and BPAc-PeNPLs dispersion. As shown in **Supplementary Fig. 10**, BPAc-PeNPLs exhibit a maximum PLQY of 65.7% and a median PLQY of 62.7  $\pm$  2.8% across 9 independently prepared samples. In contrast, pristine-PeNPLs show significantly lower values, with a maximum PLQY of 36.1% and a median value of 34.3  $\pm$  2.2% across 9 independently prepared samples. Time-resolved PL decay measurements further confirm the passivation effect of BPAc ligands.

The average carrier lifetime increases from 14.18 ns (419 μJ/cm² per pulse for excitation fluence) in pristine-PeNPLs to 21.82 ns (419 μJ/cm² per pulse for excitation fluence) in BPAc-PeNPLs (Supplementary Fig. 11). In addition, BPAc-PeNPLs exhibit negligible lifetime variation (22.22 ns to 21.82 ns) with increasing excitation fluence, whereas pristine-PeNPLs show a more pronounced decrease (15.89 ns to 14.18 ns), as summarized in Supplementary Table 1. This excitation power-dependent lifetime change suggests that pristine-PeNPLs contain a higher density of trap states, which become gradually filled at higher carrier densities, reducing nonradiative recombination. In contrast, BPAc-PeNPLs exhibit fewer trap-assisted recombination pathways, indicating effective passivation of surface defects<sup>43, 44</sup>. These findings highlight the critical role of BPAc in suppressing defect-induced nonradiative losses, resulting in improved optical properties of PeNPLs. This can be also supported by the decay curves extracted from transient absorption (TA) spectroscopy measurement for pristine and BPAc treated NPL solutions shown in Supplementary Fig. 12, where the pristine-PeNPLs show faster decay than BPAc-PeNPLs.

Experimental evidence for BPAc coordination is also observed in NMR measurements. As shown in the <sup>1</sup>H NMR spectrum (**Supplementary Fig. 13**), BPAc-treated PeNPLs display distinct peaks at approximately 7.3 ppm and 2.95 ppm, consistent with the chemical environment of the aromatic and methylene protons of BPAc molecules. Furthermore, <sup>207</sup>Pb NMR spectra (**Supplementary Fig. 14**) of BPAc-PeNPLs reveal a notable chemical shift compared to the pristine-PeNPLs, indicating altered Pb coordination environments due to BPAc ligand binding<sup>34</sup>. These experimental observations are consistent with the DFT-predicted strong binding between BPAc ligand and surface of perovskite, reinforcing the dual role of BPAc ancillary ligand as both a kinetic modulator and an effective surface passivation. Taken together, these findings demonstrate that BPAc ligands play a dual role in PeNPL synthesis by simultaneously modulating the nucleation and growth kinetics through strong coordination with Pb<sup>2+</sup> ions and effectively passivating surface defects during crystallization. This dual functionality leads to the formation of highly uniform 3ML CsPbI<sub>3</sub> PeNPLs with enhanced optical properties, including suppressed nonradiative recombination and prolonged carrier lifetimes. Such improvements in structural and photophysical properties are critical prerequisites for the formation of well-ordered, and highly-emissive PeNPL superlattices, which will be discussed in the following section.

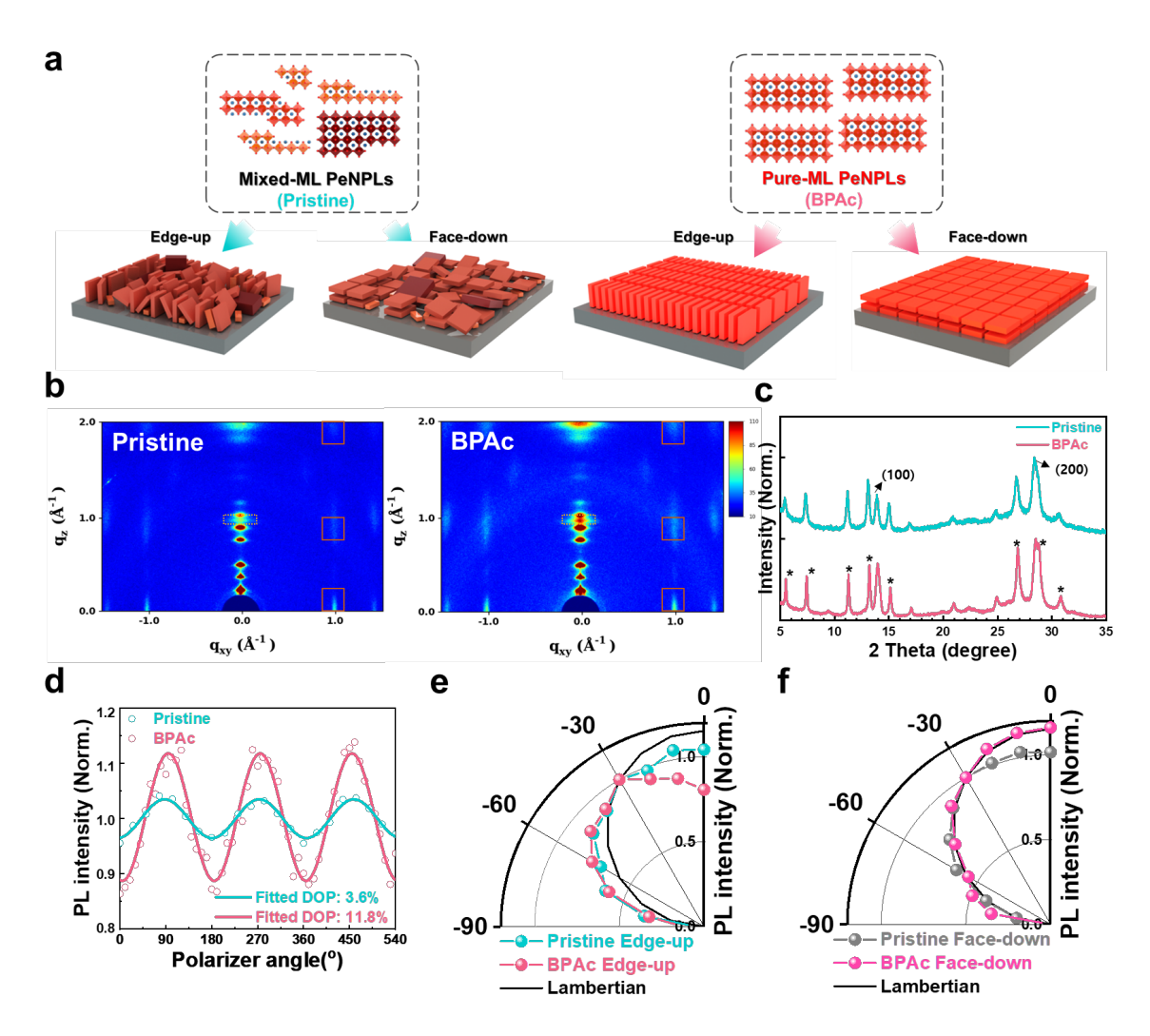


Fig. 2 | Structural characterization of superlattice formation in uniform-monolayer PeNPL films and linearly polarized emission from PeNPL superlattices

**a** Schematic illustration of the superlattice formation from mixed-ML and uniform-ML PeNPLs. **b** Grazing-incidence wide-angle X-ray scattering (GIWAXS) patterns of face-down oriented each PeNPL thin films. **c** X-ray diffraction (XRD) patterns of face-down oriented PeNPL thin films. The peaks marked with stars correspond to the multilayer diffraction pattern. **d** Polarization angle dependence of normalized PL intensity of pristine- and BPAc-PeNPL thin films, fitted with sine functions. Lambertian profile and angular distribution of the normalized PL intensity of **e** edge-up orientated pristine- and BPAc-PeNPL thin films, **f** face-down orientated pristine- and BPAc-PeNPL thin films.

### Formation and characterizations of PeNPL superlattices

To further evaluate the structural properties of the synthesized PeNPLs, we investigated their thin film assemblies and the formation of superlattices. Depending on the dispersion solvent used, the orientation of PeNPLs either edge-up or face-down can be modulated by differences in solvent evaporation rates,

which are governed by the vapor pressure of the alkanes<sup>17, 22, 45</sup>. A schematic illustration of the selfassembly of PeNPLs is shown in Fig. 2a, where BPAc-PeNPLs, due to their narrow size and thickness distribution, form highly ordered superlattices. In contrast, pristine-PeNPLs, with broader size and shape variations, exhibit disordered and randomly stacked superlattices. To characterize the structural orientation and periodicity of the PeNPL superlattices, grazing-incidence wide-angle X-ray scattering (GIWAXS) measurements were conducted (Fig. 2b and Supplementary Fig. 15). Each PeNPL thin film was fabricated by spin coating colloidal PeNPL dispersions in octane and hexane, which preferentially promote face-down and edge-up orientations, respectively. As a result, BPAc-PeNPL thin films exhibited a series of well-defined out-of-plane diffraction peaks corresponding to the (100), (101), and (102) lattice planes of the perovskite structure, which were markedly sharper and more intense than those of the pristine-PeNPL thin films. The vertical spread of the diffraction features further confirms coherent layer-by-layer stacking in the BPAc-PeNPL films. One-dimensional scattering profiles extracted from the GIWAXS data (Supplementary Fig. 16) show low-angle peaks ( $q < 1 \text{ Å}^{-1}$ ), which can be attributed to periodic electron density variations between the dense inorganic slabs and the surrounding organic ligands<sup>17,46</sup>. These features were especially pronounced in edge-up oriented BPAc-PeNPL thin films, supporting the formation of superlattices with consistent interlayer spacing. To quantify the degree of orientational alignment, we further analyzed the azimuthal dependence of scattering intensity (Supplementary Fig. 17). In the BPAc-PeNPL thin films, face-down orientations exhibited stronger intensity in the low azimuthal angle range (0°-10°), while edge-up orientations showed enhanced scattering at higher angles  $(80^{\circ}-90^{\circ})$ . These patterns were significantly sharper than those of pristine samples, indicating a higher degree of orientation in both face-down and edge-up oriented PeNPL thin films due to the well-defined crystallinity of BPAc-PeNPLs. Finally, powder Xray diffraction (XRD) patterns were recorded to confirm the periodic stacking behavior (Fig. 2c and Supplementary Figs. 18-19). Both PeNPL thin films exhibited multiple satellite peaks, in agreement with prior reports on PeNPL superlattices<sup>45, 47</sup>. Notably, BPAc-PeNPL thin films showed narrower FWHM values for these satellite peaks, indicating superior long-range structural coherence and crystallinity. Collectively, these results highlight the critical role of the BPAc ancillary ligand in enabling the formation of highly ordered, structurally coherent PeNPL superlattices. As demonstrated in the preceding analyses, the well-orientated PeNPL superlattices provide a versatile platform for a variety of applications. Edge-up oriented PeNPL thin films, characterized by their high degree of inplane dipole alignment, are advantageous for achieving strong linear polarization in light emission. In contrast, face-down oriented PeNPL thin films, with their efficient out-coupling effect, are suitable for LED devices, where maximizing light extraction is essential<sup>48, 49, 50</sup>. These orientation-dependent properties will be further explored in the following sections, demonstrating the broad applicability of

PeNPL superlattices in both polarization-sensitive photonic applications and efficient light-emitting devices.

### Improved superlattice assembly for high linearly polarized emission and out-coupling

Strongly confined two-dimensional PeNPL light emitters with anisotropic dimensional structures inherently exhibit linearly polarized emission, making them promising candidates for optical applications<sup>51,52</sup>. To evaluate the impact of superlattice formation and surface passivation on the linearly polarization properties, we conducted degree of polarization (DOP) measurements for edge-up oriented pristine- and BPAc-PeNPL thin films. Each PeNPL thin films were prepared by spin coating hexane dispersed PeNPLs onto glass substrates, and the measurement setup for polarization analysis is illustrated in Supplementary Fig. 20. As shown in Fig. 3d, Pristine-PeNPL films exhibited a relatively low DOP, with a maximum of 3.6% and a median of 3.4% across 5 independently prepared samples. In contrast, BPAc-PeNPL thin films displayed a significantly enhanced polarization response, with a maximum DOP of 11.8% and a median of 11.5% across 5 independently prepared samples. The corresponding DOP histogram is provided in Supplementary Fig. 21-22, with individual data points summarized. Angular distribution PL measurements of edge-up oriented each PeNPL thin films further support this trend (Fig. 2e). In these measurements, 0° corresponds to light collection normal to the thin films surface, while 90° represents collection parallel to the thin films plane. The PL intensity variation with respect to collection angle was significantly more pronounced in BPAc-PeNPL thin films than in their pristine-PeNPL thin films. This behavior indicates of enhanced dipole alignment, which can be attributed to the suppression of aggregation and improved thickness uniformity facilitated by the strong coordination between the perovskite surface and BPAc ligands, leading to the formation of well-ordered BPAc-PeNPL superlattices composed of uniform 3ML nanoplatelets in both face-down and edge-up orientations. In addition to polarization anisotropy, the angular emission profile provides further insight into the light extraction characteristics of PeNPL thin films. As shown in Fig. 2f, the angular distribution of the normalized PL intensity from face-down oriented BPAc-PeNPL thin films closely follows a Lambertian profile, in contrast to the more directional emission observed in face-down oriented pristine-PeNPL thin films. This improved angular emission pattern suggests more efficient light extraction, which is particularly advantageous for LED applications<sup>48, 49, 53</sup>. The Lambertian-like emission of BPAc-PeNPL thin films highlights the role of structural uniformity and suppressed scattering in contributing to the enhanced LED device performance discussed in the later section.

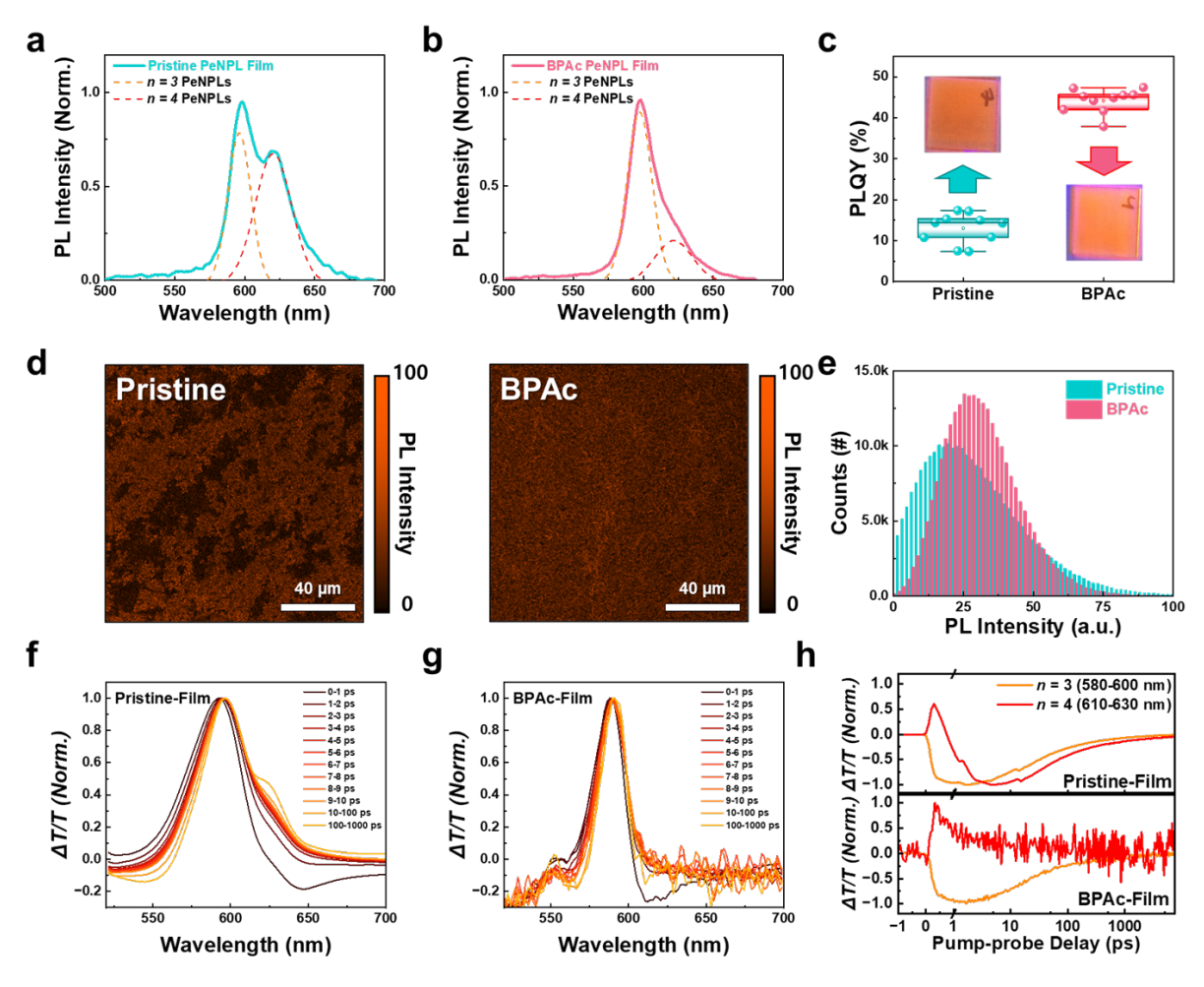


Fig. 3 | Optical characterization of PeNPL films

PL spectra of **a** Pristine-PeNPL thin films and **b** BPAc-PeNPL thin films showing contributions from 3ML and 4ML components. **c** PLQY distributions of pristine- and BPAc-PeNPL thin films. **d** Confocal PL images of each PeNPL thin film (scan area:  $120 \times 120 \ \mu m^2$ ). **e** PL intensity histograms extracted from the confocal PL mapping images. **f** Normalised TA spectra from 0-1000 ps for pristine-PeNPL films. **g** Normalised TA spectra from 0-1000 ps for BPAc-PeNPL films. **h** Decay curve of pristine- and BPAc- PeNPL films

# Optical characterization of PeNPL films

Building upon the structural insights into the PeNPL superlattice orientation, we investigated the optical characteristics of the corresponding PeNPL thin films (**Fig. 3** and **Supplementary Fig. 23**). The PL spectrum of pristine-PeNPL thin films (**Fig. 3a**) shows broadened emission with two distinct peaks at 600 nm and 627 nm, corresponding to 3ML and 4ML PeNPLs, respectively. This spectral broadening is more pronounced than that observed in the dispersion state (**Fig. 1f**), likely due to interparticle aggregation caused by ligand detachment during thin film formation due to weakly binding energy between native ligands and perovskite surface<sup>54</sup>. In contrast, BPAc-PeNPL thin films (**Fig. 3b**) exhibit

a single, narrow PL peak centered at 600 nm, indicative of emission from highly uniform 3ML PeNPLs. This uniformity can be attributed to the strong coordination between BPAc ligands and perovskite surface, which prevents aggregation and preserves size distribution even during thin film formation. PLQY measurements in the thin film state of each PeNPLs further support these observations. As shown in **Fig. 3c**, Pristine-PeNPL thin films exhibit a PLQY of 17.4% (median: 13.0% across 9 samples), significantly lower than their BPAc-PeNPL thin films. In contrast, BPAc-PeNPL thin films retain a high PLQY of 47.4% (median: 44.0% across 9 samples), showing minimal degradation upon thin film formation. This result is consistent with the passivation effects observed in the solution state measurements and confirms that BPAc ligand binding effectively suppresses nonradiative recombination pathways even in the thin film state. Spatial PL uniformity was further evaluated using confocal PL imaging (**Fig. 3d**), with the corresponding intensity histograms shown in **Fig. 3e**. Pristine-PeNPL thin films display heterogeneous emission intensity across the scanned area, reflected in a broad histogram distribution. In contrast, BPAc-PeNPL thin films exhibit significantly enhanced PL uniformity, with narrower and more symmetric intensity profiles. This homogeneity is attributed to the enhanced ML purity and strong surface passivation provide by BPAc ancillary ligand incorporation.

The monodispersity also influence the charge-carrier dynamics for PeNPL thin films. Although the presence of ligands could prevent charge transfer between different PeNPLs, the photon recycling between PeNPLs with different thickness, i.e., optical gaps, hinders the performance of the device performance. This problem is less significant in the solution, as NPLs are relatively far apart separated by the solvents. Supplementary Fig. 12a demonstrates the normalized TA spectra of the Pristine-PeNPL solution. Both the signature bleach peaks of the 3MLs (580-600 nm) and 4MLs (610-630 nm) are present in pristine-PeNPL solutions, however the relative ratio between these two peaks did not change over time, indicating there is negligible charge transfer or photon recycling happening. The decay curve for these two thickness PeNPLs also show no overlap in the early time (< 1 ns). In contrast, Fig. 3f demonstrates the normalized TA spectra of the pristine-PeNPL thin film. The ratio of the 4 MLs bleach peak increased overtime, and also there is clear decay curve overlap between two different thickness PeNPLs shown in Fig. 3h. This suggests that there is substantial charge or energy transfer between higher optical gap 3ML PeNPLs to lower optical gap 4MLs PeNPLs. This additional transfer pathway provides extra decay channel for photoexcited or electrical injected carriers, which may lower the device performance. In comparison, the BPAc-PeNPLs have more uniform size distribution. The absence of 4ML PeNPLs leads to no bleach peak of 4ML PeNPLs at 610-630 nm in both solution and film samples shown in Supplementary Fig.12b and Fig. 3g. This allows more efficient radiative recombination in BPAc-PeNPL thin film.

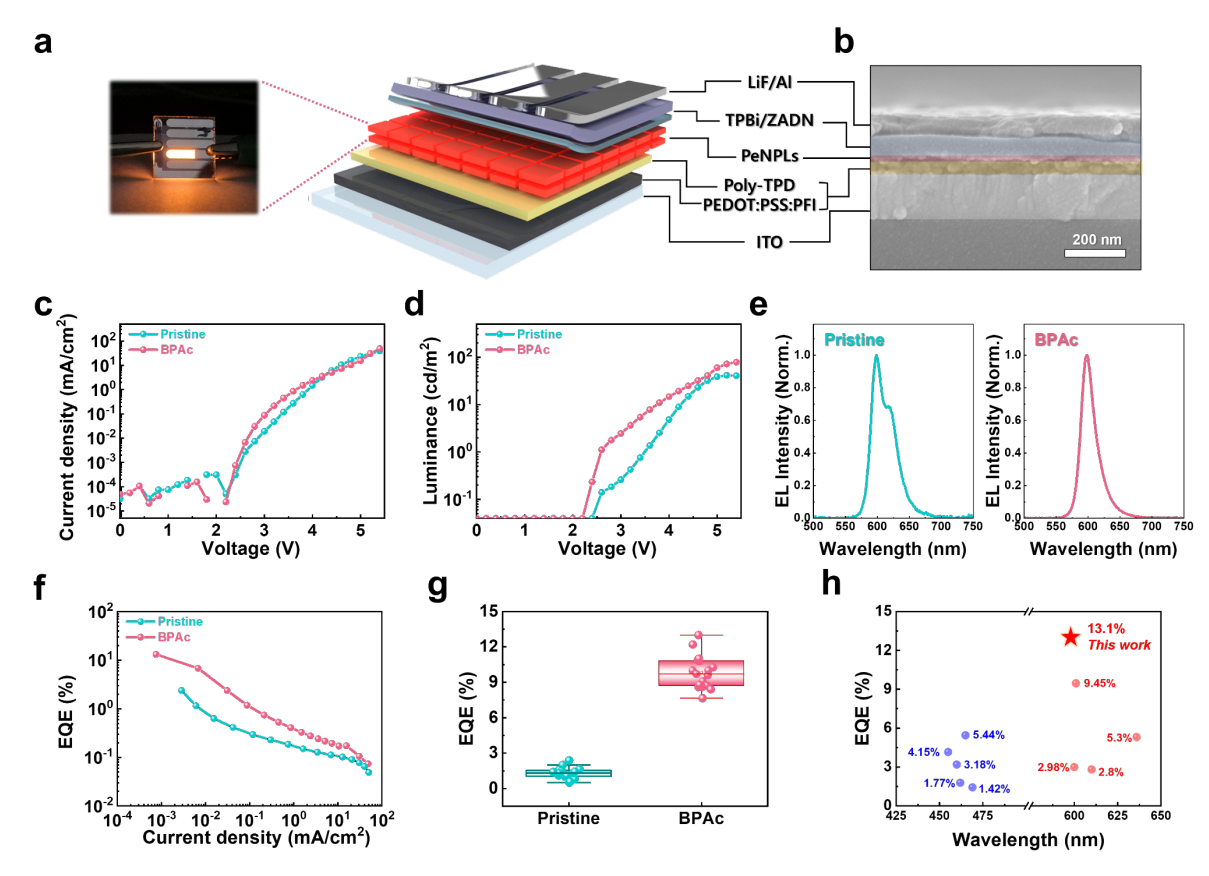


Fig. 4 | Device performance of PeNPLs.

a Device architecture, **b** Cross sectional scanning electron microscope (SEM) images of PeNPLs LED device. **c** Current density–Voltage (J-V) curve, **d** Luminance–Voltage (L-V) curve, **e** Electroluminescence (EL) spectra, **f** External quantum efficiency (EQE)–Current density (EQE-J) curve of face-down oriented pristine- and BPAc-PeNPL LED devices. **g** EQE<sub>max</sub> histogram from 17 individual PeNPL devices. **h** Comparison of the EQE<sub>max</sub> of strongly confined CsPbX<sub>3</sub> (X = I, Br) PeNPLs based LED devices with previous literature. <sup>17, 29, 30, 55, 56, 57, 58, 59, 60</sup>

Table 1. Summarized device performance parameters with pristine- and BPAc-PeNPLs champion device.

Sample configuration	EQE <sub>max</sub> [%] @ bias	L <sub>max</sub> [cd/m²] @ bias	LE <sub>max</sub> [cd/A] @ bias	Turn-on Voltage [V] @ 0.1cd/m²
Pristine-PeNPLs	2.4@2.6V	42@4.8V	5.1@2.6V	2.6
BPAc-PeNPLs	13.1@2.4V	78@5.4V	31.2@2.4V	2.4

# **Device fabrication for efficient PeNPL LEDs**

To evaluate the optoelectronic performance of the synthesized PeNPLs, we fabricated PeNPL-based

LEDs with the device architecture illustrated in Fig. 4a. The device stack consists of an indium tin oxide (ITO) transparent electrode, followed by a bilayer hole transport layer composed of PEDOT:PSS:PFI and Poly(N,N'-bis-4-butylphenyl-N,N'-bisphenyl)benzidine (Poly-TPD). The emissive layer comprises either pristine- and BPAc-PeNPLs, prepared by octane dispersed PeNPLs for face-down orientation. A bilayer electron transport structure composed of 2,2',2"-(1,3,5-benzinetriyl)-tris(1-phenyl-1-Hbenzimidazole) (TPBi) and 2-[4-(9,10-di-naphthalen-2-yl-anthracen-2-yl)-phenyl]-1-phenyl-1Hbenzoimidazole (ZADN) was deposited on top of the PeNPL layer, followed by LiF/Al as the top electrode. A cross-sectional scanning electron microscopy (SEM) image of the complete device structure is shown in Fig. 4b, confirming uniform layer stacking and a smooth interface with the PeNPL emissive layer. The orientation of PeNPLs within the thin film significantly influences device performance due to the optical out-coupling effect. Among the two orientations investigated in the previous section (edge-up and face-down orientation), the face-down orientation was selected for the primary device architecture due to its superior outcoupling in the normal direction. Comparative device performance results of edge-up oriented LEDs are provided in Supplementary Fig. 24, demonstrating slightly lower efficiency than the face-down oriented devices. This performance difference highlights the critical role of orientation in optimizing light extraction and achieving high-efficiency PeNPL-based LEDs. As shown in the current density-voltage (J-V) and luminance-voltage (L-V) characteristics (Fig. 4c and 4d), devices based on BPAc-PeNPLs exhibit improved charge injection and a lower turn-on voltage compared to pristine-PeNPL devices. This improvement is attributed to the partial replacement of long-chain, insulating native ligands in pristine-PeNPLs with shorter BPAc ligands, which enhance charge carrier mobility and facilitate stronger interparticle coupling within the emissive layer. Additionally, the well-ordered superlattice structure formed by the uniform-ML BPAc-PeNPLs promotes efficient charge transport and a uniform and narrow emission profile, as discussed in the section on PeNPL superlattice structural characterization. Electroluminescence (EL) spectra of the pristine-PeNPL and BPAc-PeNPL LED devices are shown in Fig. 4e. Pristine-PeNPL LEDs exhibited broad EL profiles with multiple emission peaks corresponding to mixed 3ML and 4ML PeNPLs, consistent with their inhomogeneous composition. In contrast, BPAc-PeNPL LEDs displayed a single, narrow EL peak centered at 600 nm, attributed to uniform 3ML PeNPL emission. This spectral purity, resulting from the improved well-controlled thickness achieved through BPAc incorporation, is further corroborated by the absence of multiple EL peaks in BPAc-PeNPL devices, confirming the structural integrity and strong exciton confinement of the PeNPL layer. The champion BPAc-PeNPL device achieved a maximum external quantum efficiency (EQE) of 13.1%, significantly surpassing the 2.4% EQE of the champion pristine-PeNPL device (Fig. 4f and Table 1). This performance was further validated by statistical analysis of 17 independently fabricated devices (Fig. 4g), demonstrating high reproducibility and a narrow distribution in EQE values. To the best of our knowledge, this value represents the highest reported EQE for strongly confined colloidal CsPbX<sub>3</sub> PeNPL-based LEDs to date (Fig. 4h). The enhanced device performance observed in BPAc-PeNPL LEDs can be attributed to several key factors. Firstly, as described above, the efficient out-coupling effect resulting from the well-aligned, face-down oriented superlattice of PeNPLs with precisely controlled shape and thickness (Fig. 2f). Secondly, the strong binding interaction of the ancillary BPAc ligands effectively passivates surface defects of the PeNPLs, reducing nonradiative losses and enhancing radiative recombination. These synergistic effects collectively contribute to the superior device performance of BPAc-PeNPL LED devices compared to their pristine-PeNPL LEDs. Overall, the successful integration of BPAc as an ancillary ligand not only enhances the device efficiency of PeNPL-based LEDs but also improves their linear polarization properties. These findings demonstrate the feasibility of ligand engineering as a promising approach to advance the development of high-efficiency, strongly confined PeNPL-based LEDs with potential applications in both high-performance LEDs and linearly polarized quantum light sources.

# **DISCUSSION**

This study reveals that the molecular architecture of the ancillary ligand introduced governs the nucleation, growth, and assembly of CsPbI<sub>3</sub> nanoplatelets through a synergistic balance between headgroup coordination and backbone steric effects. The coordination strength of the headgroup defines the nucleation barrier, while the steric profile of the backbone dictates anisotropic growth and colloidal stability. When these two factors are optimally balanced, the growth pathway converges toward uniform monolayer PeNPLs with well-passivated surfaces, providing a molecular rationale that links ligand chemistry to nanoscale morphology and photonic function. The resulting PeNPLs exhibit enhanced optical properties, suppressed nonradiative losses, and tunable optical anisotropy. By precisely controlling the orientation of the PeNPLs, we achieved a remarkable EQE of 13.1% in LED devices through improved out-coupling in face-down oriented superlattices, whereas edge-up oriented superlattices exhibit strongly linearly polarized emission suitable for quantum light sources. Overall, our findings establish a coherent design rule connecting ligand structure, nanocrystal uniformity, and device performance: select a strongly coordinating headgroup to regulate nucleation and passivation, and pair it with a backbone that provides steric stability without displacing native ligands. Looking ahead, extending this principle may enable rational control of anisotropic emission and polarizationsensitive photonic and display technologies, underscoring the broader significance of ligand engineering in strongly confined perovskite optoelectronics.

### **DATA AVAILABILITY**

Raw data for the main text and supplementary information available from the Oxford Research Archive repository [DOI to be made available before publication]

### CONFLICT OF INTERSET

The authors declare no competing interests.

### ACKNOWLEDGEMENTS

J. Y. and R. L. Z. H. thank the UK Research and Innovation for funding through a Frontier Grant (no. EP/X029900/1), awarded via the 2021 ERC Starting Grant scheme. J. Y. and R. L. Z. H. also thank St. John's College Oxford for funding through the Welcome and Large Grant schemes. R. L. Z. H. thanks the Royal Academy of Engineering and Science & Technology Facilities Council for funding through a Senior Research Fellowship (no. RCSRF2324-18-68). This work was supported by the UKRI Engineering & Physical Sciences Research Council (EPSRC; no. EP/V061747/1). This work was supported by the National Research Foundation of Korea (NRF) grant funded by the Korea government (MSIT) (RS-2025-00514448 and RS-2025-00516815) and contains the results obtained by using the equipment of UNIST Central Research Facilities (UCRF).

# **AUTHOR CONTRIBUTION**

J.K. and W.H.J. contributed equally to this work. J.K., W.H.J., J.Y. and R.L.Z.H. conceived of the ideas behind this work. J.K., W.H.J. performed formal analysis under the supervision of M.H.S., B.R.L. and R.L.Z.H., A.N.A and V. performed DFT calculations under the supervision of M.S.I. D.K. and D.L performed confocal PL microscopy. Y.-T.H. and Y.W. performed transient absorption spectroscopy under the supervision of A.R. C.-Y.C. and J.K performed the TEM measurements. X.S. and H.J.S. performed optical analysis, S.Y.B. performed XRD. J.K. and W.H.J. drafted the first version of the manuscript. J.Y., M.S.I., B.R.L., M.S. and R.L.Z.H. reviewed and revised the manuscript. This work was carried out under supervision of B.R.L., M.H.S and R.L.Z.H. All the authors contributed to the discussion of the manuscript.

### **REFERENCES**

1. Chang J, Waclawik ER. Colloidal semiconductor nanocrystals: controlled synthesis and surface chemistry in organic media. *RSC Advances* 2014, **4**(45): 23505-23527.

- 2. Ahn N, Livache C, Pinchetti V, Klimov VI. Colloidal Semiconductor Nanocrystal Lasers and Laser Diodes. *Chemical Reviews* 2023, **123**(13): 8251-8296.
- 3. Diroll BT, Guzelturk B, Po H, Dabard C, Fu N, Makke L, *et al.* 2D II-VI Semiconductor Nanoplatelets: From Material Synthesis to Optoelectronic Integration. *Chem Rev* 2023, **123**(7): 3543-3624.
- 4. Peng X, Wickham J, Alivisatos AP. Kinetics of II-VI and III-V Colloidal Semiconductor Nanocrystal Growth: "Focusing" of Size Distributions. *Journal of the American Chemical Society* 1998, **120**(21): 5343-5344.
- 5. Murray CB, Norris DJ, Bawendi MG. Synthesis and characterization of nearly monodisperse CdE (E = sulfur, selenium, tellurium) semiconductor nanocrystallites. *Journal of the American Chemical Society* 1993, **115**(19): 8706-8715.
- 6. Thanh NTK, Maclean N, Mahiddine S. Mechanisms of Nucleation and Growth of Nanoparticles in Solution. *Chemical Reviews* 2014, **114**(15): 7610-7630.
- 7. Pan D, Wang Q, An L. Controlled synthesis of monodisperse nanocrystals by a two-phase approach without the separation of nucleation and growth processes. *Journal of Materials Chemistry* 2009, **19**(8): 1063-1073.
- 8. Kim J, Kim W, Jang JI, Kim W, Yoo D, Kim JW, *et al.* SN2-mediated decoupled precursor provision enables large-scale production of monodisperse lead halide perovskite quantum dots in a single reactor. *Advanced Composites and Hybrid Materials* 2025, **8**(1).
- 9. Dey A, Ye J, De A, Debroye E, Ha SK, Bladt E, *et al.* State of the Art and Prospects for Halide Perovskite Nanocrystals. *ACS Nano* 2021, **15**(7): 10775-10981.
- 10. Huang H, Polavarapu L, Sichert JA, Susha AS, Urban AS, Rogach AL. Colloidal lead halide perovskite nanocrystals: synthesis, optical properties and applications. *NPG Asia Materials* 2016, **8**(11): e328-e328.
- 11. Mosquera-Lois I, Huang Y-T, Lohan H, Ye J, Walsh A, Hoye RLZ. Multifaceted nature of defect tolerance in halide perovskites and emerging semiconductors. *Nature Reviews Chemistry* 2025, **9**(5): 287-304.
- 12. Han S, Jeong WH, Seo G, Choi S, Lee DG, Chae W-S, *et al.* Synergistic Hybrid-Ligand Passivation of Perovskite Quantum Dots: Suppressing Reduced-Dimensionality and Enhancing Optoelectronic Performance. *Advanced Materials* 2025, **37**(25): 2410128.
- 13. Weidman MC, Seitz M, Stranks SD, Tisdale WA. Highly Tunable Colloidal Perovskite Nanoplatelets through Variable Cation, Metal, and Halide Composition. *ACS Nano* 2016, **10**(8): 7830-7839.
- 14. Otero-Martínez C, Ye J, Sung J, Pastoriza-Santos I, Pérez-Juste J, Xia Z, *et al.* Colloidal Metal-Halide Perovskite Nanoplatelets: Thickness-Controlled Synthesis, Properties, and Application in Light-Emitting Diodes. *Advanced Materials* 2022, **34**(10): 2107105.
- 15. Becker MA, Vaxenburg R, Nedelcu G, Sercel PC, Shabaev A, Mehl MJ, *et al.* Bright triplet excitons in caesium lead halide perovskites. *Nature* 2018, **553**(7687): 189-193.
- 16. Ghoshal D, Wang T, Tsai H-Z, Chang S-W, Crommie M, Koratkar N, *et al.* Catalyst-Free and Morphology-Controlled Growth of 2D Perovskite Nanowires for Polarized Light Detection. *Advanced Optical Materials* 2019, **7**(15): 1900039.
- 17. Ye J, Ren A, Dai L, Baikie TK, Guo R, Pal D, *et al.* Direct linearly polarized electroluminescence from perovskite nanoplatelet superlattices. *Nature Photonics* 2024, **18**(6): 586-594.

- 18. Shamsi J, Urban AS, Imran M, De Trizio L, Manna L. Metal Halide Perovskite Nanocrystals: Synthesis, Post-Synthesis Modifications, and Their Optical Properties. *Chemical Reviews* 2019, **119**(5): 3296-3348.
- 19. Sun S, Lu M, Lu P, Li X, Zhang F, Wu Z, *et al.* Modulation of Nucleation and Growth Kinetics of Perovskite Nanocrystals Enables Efficient and Spectrally Stable Pure-Red Light-Emitting Diodes. *Nano Letters* 2024, **24**(18): 5631-5638.
- 20. Akkerman QA, Nguyen TPT, Boehme SC, Montanarella F, Dirin DN, Wechsler P, *et al.* Controlling the nucleation and growth kinetics of lead halide perovskite quantum dots. *Science* 2022, **377**(6613): 1406-1412.
- 21. Liu H, Worku M, Mondal A, Shonde TB, Chaaban M, Ben-Akacha A, *et al.* Efficient and Stable Blue Light Emitting Diodes Based on CsPbBr3 Nanoplatelets with Surface Passivation by a Multifunctional Organic Sulfate. *Advanced Energy Materials* 2022, **13**(33).
- 22. Jeong WH, Ye J, Kim J, Xu R, Shen X, Chang C-Y, *et al.* Enhanced Stability and Linearly Polarized Emission from CsPbI3 Perovskite Nanoplatelets through A-site Cation Engineering. *arXiv* preprint *arXiv*:250522817 2025.
- 23. Litvin AP, Guo J, Wang J, Zhang X, Zheng W, Rogach AL. Systematic Study of the Synthesis of Monodisperse CsPbI3 Perovskite Nanoplatelets for Efficient Color-Pure Light Emitting Diodes. *Small* 2025, **21**(8): 2408422.
- 24. Soe CMM, Nagabhushana GP, Shivaramaiah R, Tsai H, Nie W, Blancon J-C, et al. Structural and thermodynamic limits of layer thickness in 2D halide perovskites. *Proceedings of the National Academy of Sciences* 2019, **116**(1): 58-66.
- Pun AB, Mazzotti S, Mule AS, Norris DJ. Understanding Discrete Growth in Semiconductor Nanocrystals: Nanoplatelets and Magic-Sized Clusters. *Accounts of Chemical Research* 2021, 54(7): 1545-1554.
- 26. Pathipati SR, Naeem Shah M, Mishra N. Recent advances in the synthesis and passivation of pure bromide-based perovskite nanoplatelets. *Nanoscale* 2025, **17**(23): 14035-14081.
- 27. Otero-Martinez C, Ye J, Sung J, Pastoriza-Santos I, Perez-Juste J, Xia Z, *et al.* Colloidal Metal-Halide Perovskite Nanoplatelets: Thickness-Controlled Synthesis, Properties, and Application in Light-Emitting Diodes. *Adv Mater* 2022, **34**(10): e2107105.
- 28. Huang H, Li Y, Tong Y, Yao EP, Feil MW, Richter AF, *et al.* Spontaneous Crystallization of Perovskite Nanocrystals in Nonpolar Organic Solvents: A Versatile Approach for their Shape-Controlled Synthesis. *Angew Chem Int Ed Engl* 2019, **58**(46): 16558-16562.
- 29. Chen M, Zhang T, Elsukova A, Hu Z, Zhang R, Wang Y, *et al.* Kinetically Controlled Synthesis of Quasi-Square CsPbI(3) Nanoplatelets with Excellent Stability. *Small* 2024, **20**(15): e2306360.
- 30. Litvin AP, Guo J, Wang J, Zhang X, Zheng W, Rogach AL. Systematic Study of the Synthesis of Monodisperse CsPbI(3) Perovskite Nanoplatelets for Efficient Color-Pure Light Emitting Diodes. *Small* 2025: e2408422.
- 31. De Roo J, Ibáñez M, Geiregat P, Nedelcu G, Walravens W, Maes J, *et al.* Highly Dynamic Ligand Binding and Light Absorption Coefficient of Cesium Lead Bromide Perovskite Nanocrystals. *ACS Nano* 2016, **10**(2): 2071-2081.
- 32. De Trizio L, Infante I, Manna L. Surface Chemistry of Lead Halide Perovskite Colloidal Nanocrystals. *Accounts of Chemical Research* 2023, **56**(13): 1815-1825.

- 33. Song H, Yang J, Jeong WH, Lee J, Lee TH, Yoon JW, *et al.* A Universal Perovskite Nanocrystal Ink for High-Performance Optoelectronic Devices. *Adv Mater* 2023, **35**(8): e2209486.
- 34. Kim J, Kim YI, Guo H, Lee D, Yang J, Kim D, *et al.* Toward α-CsPbI3 Quantum Dots via Dual-Functional Fluorinated Acidic Ligand. *ACS Energy Letters* 2025, **10**(9): 4402-4409.
- 35. Fiuza-Maneiro N, Sun K, López-Fernández I, Gómez-Graña S, Müller-Buschbaum P, Polavarapu L. Ligand Chemistry of Inorganic Lead Halide Perovskite Nanocrystals. *ACS Energy Letters* 2023, **8**(2): 1152-1191.
- 36. Hassan Y, Park JH, Crawford ML, Sadhanala A, Lee J, Sadighian JC, *et al.* Ligand-engineered bandgap stability in mixed-halide perovskite LEDs. *Nature* 2021, **591**(7848): 72-77.
- 37. Sun X, Yuan L, Liu Y, Shi G, Wang Y, Liu C, *et al.* Diffusion-mediated synthesis of high-quality organic–inorganic hybrid perovskite nanocrystals. *Nature Synthesis* 2025, **4**(2): 167-176.
- 38. Haydous F, Gardner JM, Cappel UB. The impact of ligands on the synthesis and application of metal halide perovskite nanocrystals. *Journal of Materials Chemistry A* 2021, **9**(41): 23419-23443.
- 39. Jeong J, Kim M, Seo J, Lu H, Ahlawat P, Mishra A, *et al.* Pseudo-halide anion engineering for alpha-FAPbI(3) perovskite solar cells. *Nature* 2021, **592**(7854): 381-385.
- 40. Protesescu L, Yakunin S, Bodnarchuk MI, Krieg F, Caputo R, Hendon CH, *et al.* Nanocrystals of Cesium Lead Halide Perovskites (CsPbX(3), X = Cl, Br, and I): Novel Optoelectronic Materials Showing Bright Emission with Wide Color Gamut. *Nano Lett* 2015, **15**(6): 3692-3696.
- 41. Jeong WH, Lee S, Song H, Shen X, Choi H, Choi Y, *et al.* Synergistic Surface Modification for High-Efficiency Perovskite Nanocrystal Light-Emitting Diodes: Divalent Metal Ion Doping and Halide-Based Ligand Passivation. *Adv Sci (Weinh)* 2024, **11**(4): e2305383.
- 42. Lee A-y, Kim J, Hyeon Jeong W, Hyun Park J, Kim D, Huang C-S, *et al.* Mitigating bulk halide defects in blue-emissive perovskite nanocrystals using benzoyl halides for efficient light-emitting diodes. *Chemical Engineering Journal* 2024, **500:** 157198.
- 43. Stranks SD, Burlakov VM, Leijtens T, Ball JM, Goriely A, Snaith HJ. Recombination Kinetics in Organic-Inorganic Perovskites: Excitons, Free Charge, and Subgap States. *Physical Review Applied* 2014, **2**(3): 034007.
- 44. Liu X-K, Xu W, Bai S, Jin Y, Wang J, Friend RH, *et al.* Metal halide perovskites for light-emitting diodes. *Nature Materials* 2021, **20**(1): 10-21.
- 45. Krajewska CJ, Kaplan AEK, Kick M, Berkinsky DB, Zhu H, Sverko T, *et al.* Controlled Assembly and Anomalous Thermal Expansion of Ultrathin Cesium Lead Bromide Nanoplatelets. *Nano Lett* 2023, **23**(6): 2148-2157.
- 46. Toso S, Baranov D, Altamura D, Scattarella F, Dahl J, Wang X, *et al.* Multilayer Diffraction Reveals That Colloidal Superlattices Approach the Structural Perfection of Single Crystals. *ACS Nano* 2021, **15**(4): 6243-6256.
- 47. Krajewska CJ, Kick M, Kaplan AEK, Berkinsky DB, Zhu H, Sverko T, *et al.* A-Site Cation Influence on the Structural and Optical Evolution of Ultrathin Lead Halide Perovskite Nanoplatelets. *ACS Nano* 2024, **18**(11): 8248-8258.
- 48. Kumar S, Marcato T, Krumeich F, Li YT, Chiu YC, Shih CJ. Anisotropic nanocrystal superlattices overcoming intrinsic light outcoupling efficiency limit in perovskite quantum dot light-emitting diodes. *Nat Commun* 2022, **13**(1): 2106.

- 49. Cui J, Liu Y, Deng Y, Lin C, Fang Z, Xiang C, *et al.* Efficient light-emitting diodes based on oriented perovskite nanoplatelets. *Science Advances* 2021, 7(41): eabg8458.
- 50. Kim J, Jung ED, You J, Lee J, Park BC, Snaith HJ, *et al.* Perovskites for next-generation colour conversion displays. *Nature Electronics* 2025.
- 51. Ye J, Gaur D, Mi C, Chen Z, Fernandez IL, Zhao H, *et al.* Strongly-confined colloidal lead-halide perovskite quantum dots: from synthesis to applications. *Chem Soc Rev* 2024, **53**(16): 8095-8122.
- 52. Ge Y, Meng L, Bai Z, Zhong H. Linearly polarized photoluminescence from anisotropic perovskite nanostructures: emerging materials for display technology. *Journal of Information Display* 2019, **20**(4): 181-192.
- 53. Zhao B, Vasilopoulou M, Fakharuddin A, Gao F, Mohd Yusoff ARb, Friend RH, *et al.* Light management for perovskite light-emitting diodes. *Nature Nanotechnology* 2023, **18**(9): 981-992.
- 54. Zheng X, Hou Y, Sun H-T, Mohammed OF, Sargent EH, Bakr OM. Reducing Defects in Halide Perovskite Nanocrystals for Light-Emitting Applications. *The Journal of Physical Chemistry Letters* 2019, **10**(10): 2629-2640.
- 55. Zhang C, Wan Q, Wang B, Zheng W, Liu M, Zhang Q, et al. Surface Ligand Engineering toward Brightly Luminescent and Stable Cesium Lead Halide Perovskite Nanoplatelets for Efficient Blue-Light-Emitting Diodes. The Journal of Physical Chemistry C 2019, 123(43): 26161-26169.
- 56. Li Z, Song Y, Cao S, Xing K, Du Z, Zou B, *et al.* Achieving a near-unity photoluminescence quantum yield and high stability of CsPbI3nanoplatelets by hydroiodic acid-assisted ligand treatment. *Inorganic Chemistry Frontiers* 2024, **11**(8): 2392-2401.
- 57. Liu H, Shonde TB, Olasupo OJ, Islam MS, Manny TF, Woodhouse M, *et al.* Organic Semiconducting Ligands Passivated CsPbBr3 Nanoplatelets for Blue Light-Emitting Diodes. *ACS Energy Letters* 2023, **8**(10): 4259-4266.
- 58. Liu H, Worku M, Mondal A, Shonde TB, Chaaban M, Ben-Akacha A, *et al.* Efficient and Stable Blue Light Emitting Diodes Based on CsPbBr3 Nanoplatelets with Surface Passivation by a Multifunctional Organic Sulfate. *Advanced Energy Materials* 2023, **13**(33): 2201605.
- 59. Shen W, Yu Y, Zhang W, Chen Y, Zhang J, Yang L, et al. Efficient Pure Blue Light-Emitting Diodes Based on CsPbBr3 Quantum-Confined Nanoplates. ACS Applied Materials & Interfaces 2022, 14(4): 5682-5691.
- 60. Wang L, Liu J, Gong Y, Yu J, Li Q, Liu Z, et al. Efficient, Color-Stable, Pure-Blue Light-Emitting Diodes Based on Aromatic Ligand-Engineered Perovskite Nanoplatelets. *Nano Letters* 2024, **24**(23): 7004-7011.